Peri-tetracene from 1,1'-bitetracene: Zipping up structurally defined graphene nanoribbons

Maren Klein,[a,b] John B. Bauer,[b] Nina Kainbacher,[c] Marie S. Wagner,[a,b] Katharina Greulich,[a] Philipp Haizmann,[a] Erika Giangrisostomi,[d] Ruslan Ovsyannikov,[d] Peter Puschnig,[c,] Thomas Chassé,[a,e] Holger F. Bettinger,[b,e,*] and Heiko Peisert[a,*]*

[a]*Institute of Physical and Theoretical Chemistry, University of Tübingen, 72076 Tübingen, Germany*
[b]*Institute of Organic Chemistry, University of Tübingen, 72076 Tübingen, Germany*
[c]*Institute of Physics, NAWI Graz, University of Graz, 8010 Graz, Austria*
[d]*Institute Methods and Instrumentation for Synchrotron Radiation Research, Helmholtz-Zentrum Berlin GmbH, 12489 Berlin, Germany*
[e]*Center for Light-Matter Interaction, Sensors & Analytics (LISA+) at the University of Tübingen, 72076 Tübingen, Germany*
*Corresponding authors: heiko.peisert@uni-tuebingen.de, holger.bettinger@uni-tuebingen.de, and peter.puschnig@uni-graz.at

Electronic Supplementary Information (ESI) available: NMR spectra, Additional STM and LEED images, structural model of adsorption place, peak fit data, additional ARPES bandmaps, NEXAFS spectra. See DOI: 10.1039/x0xx00000x

ABSTRACT

Polycyclic aromatic hydrocarbons (PAH) are promising molecules for a manifold of applications in organic electronics, spintronics or energy storage devices. Among PAHs, particular attention has been focused on the synthesis and study of acenes and fused acenes - *peri*-acenes -, allowing a tuning of the HOMO – LUMO gap with the size of the conjugated system. As a starting point for surface synthesis of larger PAHs, we synthesized a 1,1'-bitetracene for the first time. This precursor molecule consists of two tetracene units connected via the 1,1'-position with a torsion angle of 70°. Interface properties of the molecule before and after annealing on a Cu (111) surface are investigated. Using X-ray photoemission spectroscopy (XPS), angle-resolved photoelectron spectroscopy (ARPES), low-energy electron diffraction (LEED), scanning-tunneling microscopy (STM), it is experimentally demonstrated that the tetracene units zip up with the help of heat forming *peri*-tetracene. These results and the exact adsorption geometry are in excellent agreement to calculations using density functional theory (DFT). Moreover, the calculations enable the identification of newly formed valence band states at the interface to Cu (111).

1. Introduction

Band gap opening and engineering of nanographenes has attracted enormous attention in the context of the development of graphene electronics, optoelectronics, and spintronics.[1-4] Such nanoscale graphene fragments have a high potential as organic semiconductor materials, as they enable tunable bandgaps.

An important class of nanographene molecules are acenes and *peri*-acenes (PA), which are promising candidates for applications in organic spintronics, organic field effects transistors (OFETs), or organic light-emitting diodes (OLEDs).[1-4] Acenes consist of linearly fused benzene rings and have unique electronic properties.[5-7] *Peri*-acenes exhibit a two-dimensionally enlarged π-conjugated electron system that results from the lateral fusion of two acene molecules.[8]

While the smallest *peri*-acenes namely perylene (2-PA) and bisanthene (3-PA) were synthesized by Scholl et al.[9] in 1910 and Clar in 1948,[10] respectively, the synthesis of higher *peri*-acenes evokes some challenges. The first higher PA ($n \geq 4$, with n denoting the number of benzene rings along the zigzag axis), 5-PA, was detected as side-product by mass spectrometry only in 2005.[11] To circumvent the intrinsic reactivity in solution-based synthesis, two main strategies have been established. Either, the reactive sites are blocked sterically providing kinetic stabilization,[12-14] or thermodynamic stabilization is induced by heteroatom substitution.[15-18] Kinetically stabilized *peri*-tetracene (n = 4) and *peri*-heptacene (n = 7) have small gaps and limited lifetime in solution.[12-14] The singlet-triplet energy gap of 2.5 kcal mol^{-1} reported[13] for a substituted *peri*-tetracene is much smaller than that of tetracene (29.5 kcal mol^{-1})[19] and is indicative of diradical character.[4, 20-24]

Since solution-based synthesis routes of unsubsituted *peri*-acenes with $n \geq 4$ have not been successful so far, on-surface synthesis under UHV conditions is an attractive alternative. By depositing appropriate precursor molecules, which can undergo oxidative ring-closure or cyclodehydrogenation catalyzed by a metal substrate, *peri*-acenes can be prepared on the surface. This has been shown for 4-PA,[25] 5-PA,[26-27] and recently for 7-PA[28] (**Figure 1a**). In these works, using scanning tunneling microscopy (STM) and non-contact atomic force microscopy (nc-AFM), the respective atomic arrangements of *peri*-acenes were characterized. Scanning tunneling spectroscopy (STS), in addition to spin-polarized density functional theory calculations revealed the electronic structures. Due to its polyradical character *peri*-acenes show strong interactions with the surface,[29-30] which results in enhanced screening and a lower energy gap.[31]

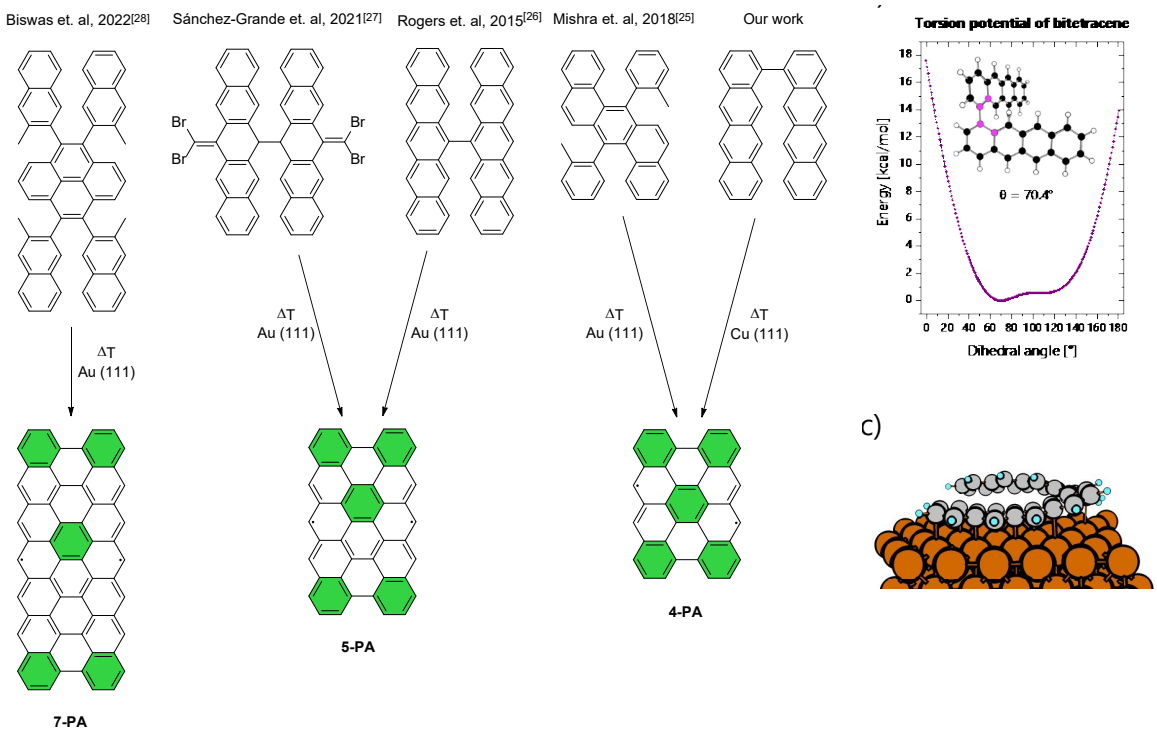

Figure 1: (a) Precursor molecules (top) which undergo surface-assisted cyclodehydrogenation to n-PA (bottom). All *peri*-acenes present a diradical singlet ground state. Green-filled benzene rings denote Clar sextets. (b) The Bi4A molecule has a minimum energy at a dihedral angle of ~70° according to computations at the r^{2}SCAN-3c level of theory.[32] The dihedral angle between the two tetracene wings (marked in pink) was varied in steps of 1°. (c) The computed adsorption configuration after deposition of a Bi4A molecule on a clean Cu (111) crystal is displayed.

Previous on-surface syntheses of *peri*-acenes were performed on Au (111) starting from submonolayer coverages of the different precursor molecules (cf. **Figure 1a**).[25-28] Individual molecules were studied by STM, STS, and AFM, particularly in the presence of by-products of the cyclodehydrogenation.

Generally, the assembly, structure, and electronic properties of monolayer films on surfaces are responsible for the energy level alignment or determine the growth and structure of multilayer thin films, which is relevant for integration into optoelectronic devices. We achieve the on-surface synthesis of *peri*-tetracene using 1,1'-bitetracene (Bi4A, $C_{36}H_{22}$) as a precursor on a Cu (111) crystal. This alternative starting material leads us to a broader set of compounds for the synthesis of unsubstituted peri-acenes. This molecule consists of two tetracene wings at a torsion angle of around 70° (**Figure 1b**). The adsorption configuration of Bi4A on Cu (111) (**Figure 1c**) will be discussed in context with experimental and computational results. We show that surface and temperature assisted cyclodehydrogenation close the C-C bonds at the *peri* positions and thus zips up *peri*-tetracene. In fact, such graphene zipping reactions are already known.[33-35] Another example are zipping reactions on Au(111) surface, in which the C–F and C–H activations take place.[36] But a detailed analysis of the geometric and electronic structure was not reported for any *peri*-acene monolayer so far. We here close this gap and follow this on-surface reaction by core level photoelectron spectroscopy and angle-resolved photoelectron spectroscopy (ARPES), that images valence states. Together with additional work function measurements we were able to calculate the ionization potential (IP) and electron affinity (EA) of Bi4A. In addition to STM measurements on a

Cu (111) crystal, we could also receive a low-energy electron diffraction (LEED) pattern of the now-formed 4-PA.

2. Methods

The Cu (111) single crystal was cleaned by several cycles of Ar^+-ion sputtering at a voltage of 1 kV for 15 min at an argon pressure of $5 \cdot 10^{-5}$ mbar and subsequent annealing to 500 °C for 20 min. The cleanliness and orientation of the crystal were checked by X-ray photoelectron spectroscopy (XPS), ultraviolet photoelectron spectroscopy (UPS), scanning tunneling microscopy (STM) and low-energy electron diffraction (LEED).

The Bi4A molecules were evaporated from a Knudsen cell at rates of 0.1 – 0.3 nm/min determined by a quartz crystal microbalance (QCM). During evaporation, the single crystal was held at room temperature. The monolayer was subsequently annealed to 250 °C for 30 min to achieve cyclodehydrogenation. All values of the film thickness were obtained by a comparison of photoemission intensities between the substrate and the overlayer-related peaks, assuming layer-by-layer growth. Atomic cross sections were taken from Yeh and Lindau[37] and mean free paths for organic molecules were calculated according to Seah and Dench.[38] According to the crystal structure of the related pentacene, the molecule-to-molecule distance in vapor-deposited crystals is about 0.35 nm.[39] Assuming that the molecules do not lie completely flat, the thickness of a (nominal) monolayer (ML) was estimated to be 0.45 nm.

Photoemission (PES) measurements in the home-lab were performed in a multichamber ultrahigh vacuum system equipped with a hemispherical energy analyzer (Phoibos 150, SPECS), an X-ray source (Al Kα radiation, hν = 1486.7 eV) with monochromator (XR 50 M, SPECS) as well as an UV radiation source (UVS 300, SPECS). For UPS measurements, the excitation energy of He I (21.2 eV) and He II (40.8 eV) were used. The photoemission spectra were calibrated by reproducing the binding energies (BE) of Au $4f_{7/2}$ and Cu $3p_{3/2}$ at 84.00 eV and 932.56 eV, respectively. Core-level spectra were fitted by using Unifit 2018.[40] A Shirley model background and a Voigt profile (convolution of Lorentzian and Gaussian profiles) were used. The Lorentzian width for C 1s core-level was set at 0.10 eV, according to the literature.[41] The error on the absolute binding energies is estimated to be less than ± 0.05 eV. For the description of the asymmetric peak shape of C 1s core levels the Doniach-Sunjic-peakshape[42] was used.

Energy-momentum intensity maps were acquired at the PM4 beamline of the synchrotron storage ring BESSY II (Berlin) using the ARTOF analyzer of the LowDosePES endstation.[43]

STM and LEED measurements were performed in a two-chamber UHV system equipped with a LEED/AES spectrometer (OCI Vacuum Microengineering Inc.) and a variable temperature (VT)-STM (Omicron NanoTechnology GmbH). For the STM measurements, mechanically cut Pt/Ir tips were used. The sample and the tip were held at room temperature, and all tunneling voltages were referenced to the sample. On the STM images displayed in this work, no filtering or smoothing procedure was applied. The WSxM program[44] was used to enhance the image contrast and the brightness of the shown STM images. For LEED analysis, the program LEEDpat[45] was used.

Quantum chemical calculations of isolated molecules were performed with the ORCA package.[46] Geometry optimizations employed the global hybrid B3LYP functional,[47-48] in combination with the def2-TZVP basis set.[49] The DFT calculations for the on-surface geometry optimizations were done with the Vienna ab-initio simulation package (VASP)[50-52] with an GGA-PBE[53] exchange-correlation

functional and the DFT-D3(zero) method of Grimme[54] for van der Waals corrections. The projector-augmented-wave (PAW) method was used for the description of the core electrons and a 400 eV energy cut-off. Making use of the repeated slab approach for the interface simulation,[55] the substrate was simulated by 6 layers of copper and a vacuum gap of around 20 Å in z-direction was introduced between the slabs. The calculations were performed on a 2x2x1 Monkhorst-Pack k-grid[56] using damped molecular dynamics for the structure relaxation until the forces were below 0.01 eV/Å. For the molecular orbital projected density of states (MOPDOS), the hybrid functional HSE06 with the same van der Waals correction scheme and k-grid were used.

3. Results and Discussion

3.1. Synthesis and optical characterization

The synthesis of 1,1'-bitetracene (Bi4A) starts from commercially available bromoxylene (**1**) that was brominated at the benzylic positions with N-bromosuccinimide (NBS) (**Scheme 1**). This yielded compound **2**, along with more highly brominated compounds. This mixture of benzylic brominated compounds was transformed into the *ortho*-quinodimethane derivative that in turn formed the tetracene scaffold **3** via Diels-Alder reaction with 1,4-naphtoquinone. Subsequent reduction of the quinone with $NaBH_4$ in *iso*-propanol gives 1-bromotetracene (**4**). The synthesis of **4** thus follows that of 2-bromotetracene reported earlier.[57]The cross-coupling of **4** using bis(cyclooctadiene)nickel [$Ni(COD)_2$] provided 1,1'-bitetracene (Bi4A, **5**) as an orange solid similar to tetracene (4A). Bi4A also shows similar solubility in organic solvents as 4A, which is in stark contrast to 2,2'-bitetracene that is essentially insoluble in organic solvents.[58] It was therefore possible to fully characterize Bi4A with solution phase NMR methods as well as with mass spectrometry.

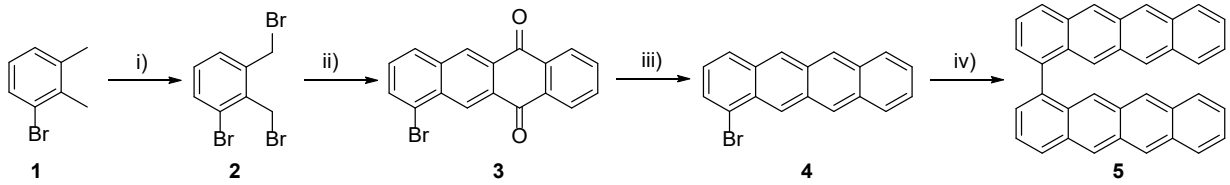

Scheme 1: Synthesis of 1,1'-bitetracene (Bi4A). Reagents and conditions: (i) NBS, AIBN, DCM, 50 °C, 72 h (ii) 1,4-naphthoquinone, NaI, DMF, 110 °C, 48 h, 37 % for i) and ii); (iii) NaBH4, i-PrOH, 75 °C, 40 h, 82 %; (iv) glovebox: Ni(COD)2, 2,2'-bipyridine, COD, THF, RT, 20 h, 90 %.

The UV/Vis spectrum (**Figure 2**) of Bi4A and 4A are very similar. For Bi4A, the longest wavelength absorption band and the maxima of the vibrational progression of the ^1L_a band according to Platt[59] are at λ_{max} = 482, 451, 424, and 400 nm. This corresponds to distances of the progression bands of 1426, 1412, and 1415 cm^{-1}, which are comparable to those of 4A, and indeed typical for acenes.[60] The UV/Vis spectrum of Bi4A is bathochromically shifted compared to that of 4A by 252 cm^{-1} – 1370 cm^{-1} in the wavelength range from 350 to 500 nm. In contrast, 2,2'-bitetracene investigated by Pflaum et al. in anthracene single crystals shows no shifts in the absorption spectrum indicating that the tetracene chromophores retain their spectral properties in the 2,2'-dimer.[58]

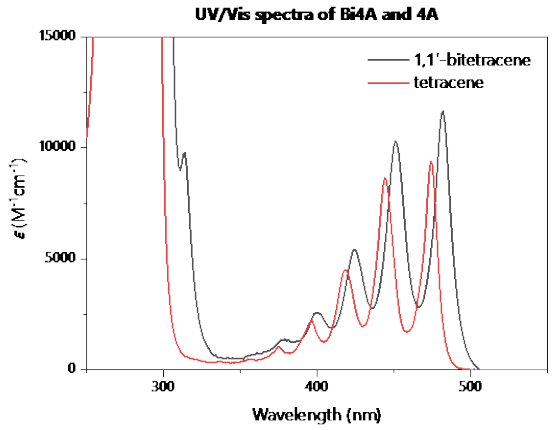

Figure 2: Absorption spectra of Bi4A and 4A measured in DCM at 25 °C (c=6.8·10^{-6} mol/L).

The molar extinction coefficients of Bi4A (ε_{482nm} = 12000 $M^{-1}cm^{-1}$) and 4A (ε_{474nm} = 9300 $M^{-1}cm^{-1}$) measured in DCM at 25 °C have comparable values (**Table 1**). For dimers consisting of electronically non-interacting tetracenes, Bi4A would be expected to have an extinction coefficient approximately twice that of 4A.[61] Thus, the relatively similar extinction coefficients of Bi4A and 4A are an indication of electronic coupling of the chromophores in Bi4A. The absorption spectra at the highest and lowest concentration of tetracene and bitetracene in DCM at room temperature are shown in **Figure S8**.

Table 1: Maxima of the absorption bands and corresponding extinction coefficients measured in DCM at 25 °C.

	UV/Vis λ_{max} [nm] (ε [$10^4 M^{-1}cm^{-1}$])
Bi4A	482 (1.18), 451 (1.04), 424 (0.53), 400 (0.24), 300 (4.20), 289 (11.80), 274 (16.81)
4A	474 (0.93), 444 (0.86), 418 (0.46), 396 (0.15), 296 (2.59), 278 (27.56) 268 (8.26)

3.2. Interface properties between Bi4A and Cu (111)

The energy level alignment (ELA) was determined for Bi4A multilayers on Cu (111) using UV photoelectron spectroscopy (UPS) (**Figure 3**). Various effects can affect the measured work function of molecules on a clean metal surface, including image charge screening, chemical interaction between substrate and adsorbate, geometry changes of the molecules, or interfacial charge rearrangements.[62-64] Since in the case of monolayer coverages strong interactions at interfaces may affect distinctly basic electronic parameters, especially the ionization potential,[65] we take multilayer films for the determination of the ELA. The valence band spectrum of a Bi4A multilayer of 2 nm thickness and that of the bare Cu (111) substrate were obtained at normal emission (excitation energy of He I, 21.2 eV). The measured work function Φ of Cu (111) (**Figure 3a**, left side), is in good agreement with the literature[66] (also cf. **Table 2**). The work function is defined as the energetic difference between the vacuum level E_V close to the surface and the Fermi level E_F.

The ELA can be directly inferred from the valence band spectra (**Figure 3a**). We assign the first emission with the intensity maximum at 2.0 eV to the HOMO. Note that in this multilayer film, no features arising from copper are visible anymore. To determine the HOMO position with respect to the Fermi level of the substrate, the onset of the HOMO obtained by a linear extrapolation was taken (1.40 eV). Together with the work function, we obtain the ionization potential IP = $HOMO_{onset} + \Phi$ = 5.33 eV. This corresponds to the adiabatic ionization potential since no geometric relaxation occurs in the time scale of photoemission. Considering the bandgap of E_{gap} = 2.68 eV obtained from DFT computations using the B3LYP functional with the def2-TZVP basis set for the isolated molecule, we can derive an estimate for the electron affinity E_A of 2.52 eV. These data can be put in relation to experimental values of a tetracene (4A) molecule on a dielectric substrate (E_A = 2.56 eV, IP = 5.2 eV).[67]

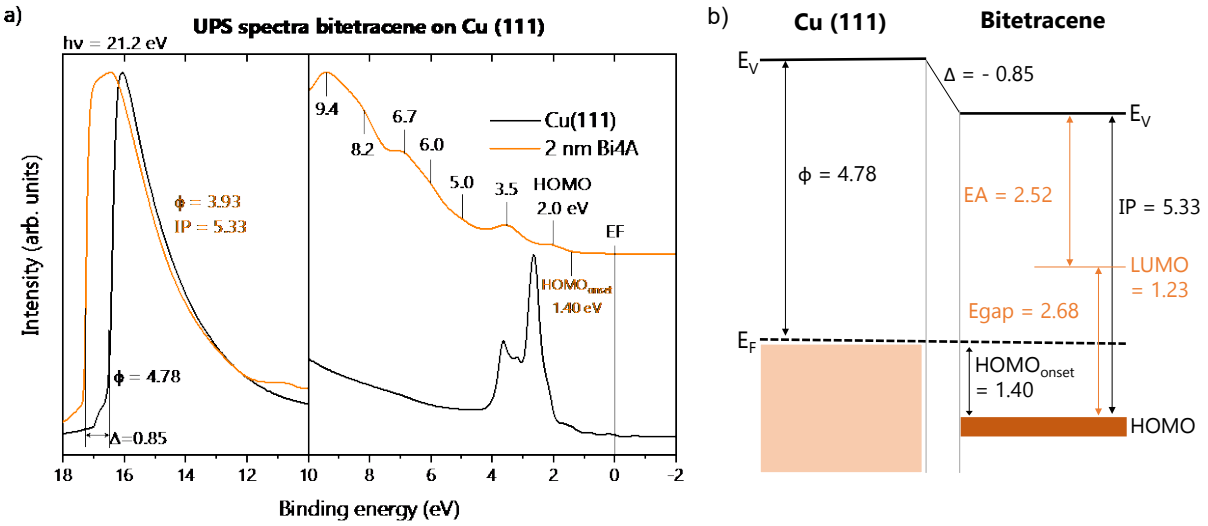

Figure 3: (a) UPS valence band spectra of Bi4A multilayer coverage on Cu (111) and the bare substrate (b) Energy level alignment of Bi4A multilayer on Cu (111) as obtained from UPS (black values) and DFT (orange values). All values are given in eV.

Table 2: Experimentally determined work functions for a multilayer deposition and computed work function changes for the hollow-hcp adsorption site with 0° rotation for a monolayer deposition Bi4A on Cu (111).

	calculation [eV]	**experiment [eV]**
$\phi_{Cu(111)}$	4.76	4.78
ϕ_{Bi4A}	3.94	3.93
$\Delta\phi$	- 0.82	- 0.85
$\Delta\phi_{bond}$	- 0.74	-
$\Delta\phi_{bend}$	- 0.04	-
$\Delta\phi_{surf}$	- 0.01	-

Table 2 lists the individual contributions to the total work function change $\Delta\phi$ computed using DFT. The most significant part of the work function change is due to charge rearrangements ($\Delta\phi_{bond}$) upon adsorption. Additional small amounts are attributed to bending/distortion of the molecule ($\Delta\phi_{bend}$)

and to small rearrangements of the metal atoms ($\Delta\phi_{surf}$) upon adsorption. The DFT derived overall changes in the work function were found to be in very good agreement with the experimental result. Note, that the experimental values were derived from multilayer coverage Bi4A, while the calculated values are for a monolayer deposition. This can be compared, if the interface dipole is essentially formed after monolayer deposition and a vacuum level alignment occurs for subsequent layers. Additional experimental data for 2 layers of Bi4A deposited on Cu (111) suggest that this is indeed the case (**Figure S13,** Supporting Information) as the deviation is about 0.03 eV.

The bond dipole contains contributions of both the competing Pauli push-back effect (negative) and interfacial charge transfer (positive in the case of an electron transfer to the molecule). For a related system (heptacene on Cu (100)),[68] it was demonstrated that the size of the push-back may even exceed the charge transfer contribution. Thus, the sign of the bond dipole in **Table 2** is no indication for the direction of the electron transfer.

3.3. Monolayer coverages of Bi4A on Cu (111) and the effect of annealing

3.3.1. Spectroscopic characterization

The interaction of π-conjugated molecules with coinage metal surfaces like copper may change the electronic structure distinctly because of charge transfer and chemisorption.[69-72] In some cases even chemical reactions were observed.[73-74]

Valence-band spectra of monolayer coverages were taken from integrated energy-momentum angle-resolved photoemission spectra (ARPES) at an excitation energy of 40 eV. This excitation energy was chosen to optimize the ratio of photoemission cross sections of C 1s and Cu 3p core levels, and the surface sensitivity. Since the intensity of valence band features is angular dependent, the sample was rotated by 30° with respect to normal emission (polar angle θ=30°). This affects the wave vector $k_{||}$, which is a function of θ at constant kinetic energy E_{kin} of the free photoelectrons.[75] Choosing θ=30°, regions with maximal HOMO intensities for related π-conjugated molecules are covered (cf., e.g. Ref.[76]). The enlarged view of the low-binding-energy region of angular integrated valence band spectra of a monolayer Bi4A on Cu (111) before and after annealing (**Figure 4a**) shows characteristic features, which we assigned with the help of calculations. In particular, according to the molecular orbital projected density of states (MOPDOS), the features between 1.6 and 1.3 eV for the Bi4A monolayer spectrum before annealing (**Figure 4a**, top panel) can be attributed to the highest occupied molecular orbital HOMO and HOMO-1 of Bi4A. The broad emission at lower binding energies can be assigned to the (former) lowest unoccupied molecular orbital (LUMO) in the free molecule, which becomes occupied at the interface.

After annealing of a Bi4A monolayer to 250 °C, the intensity distribution in the valence band region changes drastically (**Figure 4a**, bottom panel): The features around 1.45 eV disappear, and a new, intense feature peaked at 0.9 eV with a tail towards lower binding energies develops. According to MOPDOS calculations, this state cannot be attributed to Bi4A anymore, but is in excellent agreement to the expected energetic positions and intensities of the HOMO and filled LUMO of 4-PA on Cu (111), with the LUMO and HOMO centered at 0.75 eV and 0.9 eV, respectively. Corresponding energy-momentum ARPES intensity maps of a monolayer deposition Bi4A on Cu (111) before and after annealing (**Figure S12**) clearly show some additional intensity at a wave vector of 1.5 $Å^{-1}$ and a binding energy of 0.9 eV. The MOPDOS calculations confirm that a charge transfer from the substrate to the newly formed 4-PA molecule occurs, resulting in the occupation of the 4-PA LUMO. In contrast to that, the surface dipole is significantly reduced due to the Pauli pushback effect, which in turn leads to a reduction in the work function compared to the clean Cu (111) surface (**Figure 4b**).

However, annealing leads to an increase of the work function by almost 0.3 eV compared to the unheated layer. The C1s binding energy is simultaneously reduced by 0.7 eV with respect to E_F (see below). This reduces the binding energy with respect to the vacuum level or the C1s ionization energy by about 0.4 eV, which indicates a chemical modification.

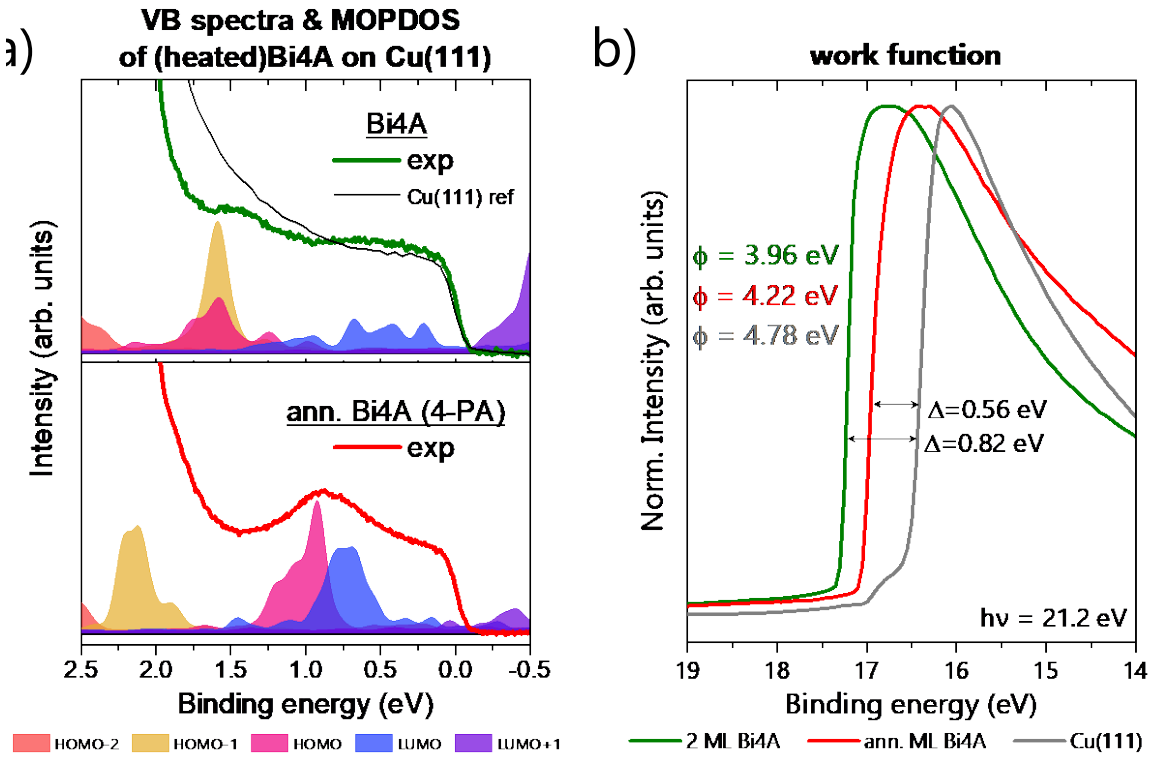

Figure 4: Integrated energy-momentum ARPES spectra (hν = 40 eV) (lines) and calculated molecular orbital projected density of states (MOPDOS) (filled areas) of a monolayer coverage Bi4A on Cu (111) before (top) and after (bottom) annealing. The experimental spectra are compared to the MOPDOS of Bi4A (before annealing) and 4-PA (after annealing) (a). Measured work functions of the clean Cu (111) surface, 2 ML of Bi4A, and an ann. ML Bi4A on the Cu (111) substrate obtained at normal emission and an excitation energy of He I, 21.2 eV) (b).

Energy-momentum intensity maps for the clean Cu (111) surface and a ML coverage of Bi4A (before and after annealing) on the Cu (111) are shown in **Figure 5**. To enhance the relative intensity of substrate-related features, a higher excitation energy of 75 eV was chosen than in **Figure 4a** (cf. photoionization cross sections, Ref.[37]). The clean Cu (111) surface exhibits the characteristic Shockley-state (red arrow in **Figure 5**a), which arises due the termination of the Cu single crystal that affects the electronic structure at the surface. The Shockley state disappears almost after deposition of Bi4A and is also hardly visible for the Bi4A monolayer on Cu (111) (**Figure 5b,c**). The almost complete disappearance indicates that the electronic structure of the Cu (111) surface has been changed upon the adsorption of Bi4A. Thus, this observation supports the scenario of a charge transfer from Cu to the (annealed) Bi4A monolayer, as concluded from valence band spectra (cf. **Figure 4a**, the LUMO is filled in both cases).

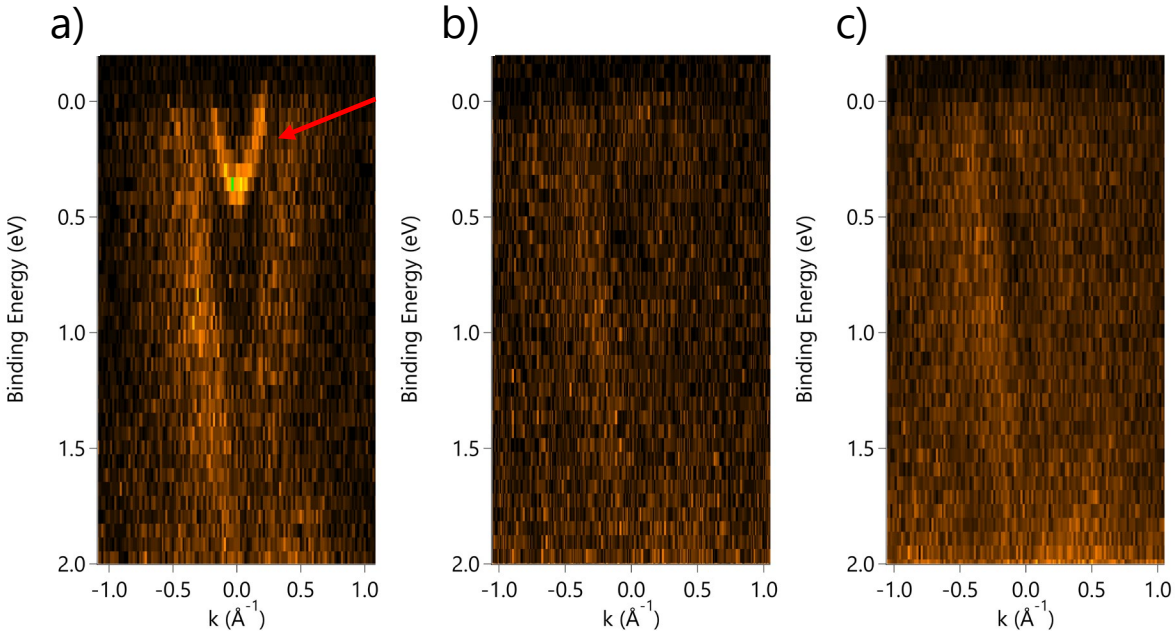

Figure 5: Energy-momentum ARPES intensity maps (obtained at normal emission) of a clean Cu (111) surface with a pronounced Shockley-state (red arrow) (a), a ML Bi4A/Cu (111) (b) and an annealed ML Bi4A/Cu (111) (c) at an excitation energy of hν = 75 eV. The strongly suppressed Shockley-state in b) and c) indicates a strong electronic coupling of the molecules with the copper surface.

Further evidence for strong interactions or even chemical reactions can be obtained from core level photoelectron spectroscopy. C 1s core level spectra of a monolayer of Bi4A on Cu (111) before and after annealing show a distinct shoulder at the low binding energy side, which is typical for larger acenes on copper surfaces[77] (**Figure 6)**. The core level spectra can essentially be described by two components, assigned to C-C and C-H species. In agreement with further reports on acenes[78-79] and graphene nanoribbons,[80] the C-H components appear at a lower binding energy compared to the C-C components. An asymmetric Doniach-Sunjic peak shape has to be applied, which indicates strong electronic coupling with the metallic substrate.[42] Further XAS spectra (Supporting Information, **Figure S14**) point to a planarization of the Bi4A molecule already before annealing which is in good agreement with the DFT-optimized adsorption structure of Bi4A / Cu (111) (**Figure 1c**).

In addition, the peak fit in **Figure 6** reveals that the relative intensity of the low binding energy component decreases distinctly upon annealing. This implies that the number of C-H atoms is decreased as expected for a gradual progress of a chemical reaction from Bi4A to 4-PA. Moreover, a significant peak shift is visible: The binding energy of the main component decreases from 284.8 eV before to 284.1 eV after annealing. A possible reason is the chemical reaction and a filling of the LUMO of 4-PA, as already discussed in commenting the valence band spectra.

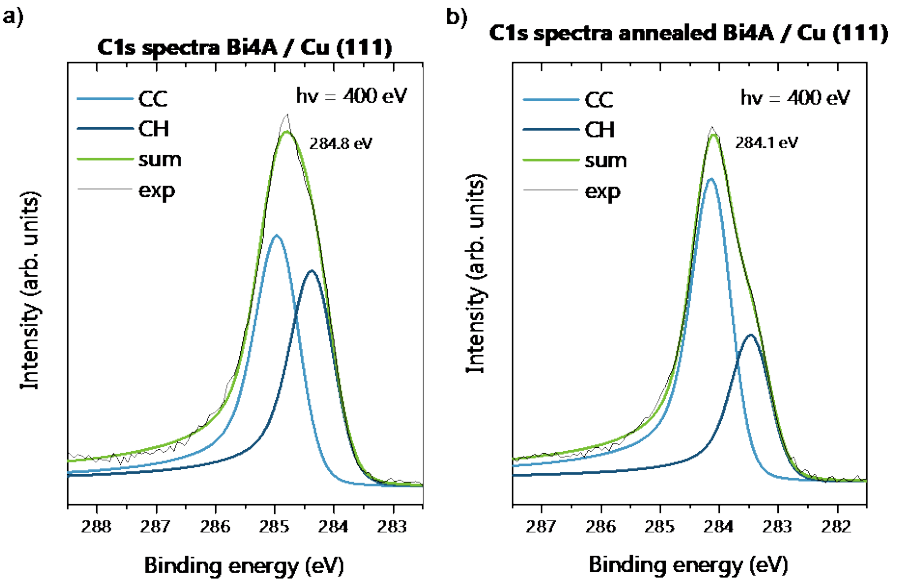

Figure 6: C 1s core-level spectra fitted with two different components (carbon bond to carbon (CC) and carbon bond to hydrogen (CH)) according to DFT calculations of a monolayer Bi4A before (a) and after (b) annealing to 250 °C.

In summary, photoelectron spectroscopic measurements indicate that upon annealing a cyclodehydrogenation of Bi4A occurs and most probably 4-PA is formed. Its formation is further substantiated by additional investigations discussed in the following sections.

3.3.2. Confirmation of the surface-assisted formation of 4-PA by STM and LEED

To confirm a possible surface-assisted cyclodehydrogenation of Bi4A to 4-PA on copper surfaces, STM and LEED measurements were performed for the monolayer annealed to 250 °C (**Figures 7** and **8**). The STM image of a large surface area (**Figure 7a**) clearly shows the formation of regions with a high ordering (dark rectangles). Within these regions the molecules arrange in three different directions, which are related to the threefold crystal symmetry. This is discussed in detail together with the LEED images below (**Figure 8**). The STM image in **Figure 7b** shows a smaller area in a particular well-ordered region. In this region only a single domain is observed; the molecules are arranged along the $[\bar{1}10]$ direction of the substrate. A closer inspection of the arrangement by a line profile (black line in **Figure 7b**) confirms the already observed periodicity. The apparent height of the molecules is about 60 pm, distinctly less than expected for a flat lying molecule, which may indicate that the separation between the molecules is small and thus the correct distance to the substrate surface is not imaged. Most importantly, the distance between two valleys in the line profile of **Figure 7c**, drawn in the direction of the shorter molecular axis, is significantly larger than expected for a single acene molecule. In addition, the molecules appear comparably planar and not twisted as expected for Bi4A (see above). A high disorder of the molecules is probably responsible for the fact, that no structures could be recognized in the STM (cf. **Figure S9**).

Rather, the distance between the valleys in **Figure 7c** is in good agreement with the expected width of a *peri*-tetracene (4-PA) molecule (**Figure 7d)** which was calculated for the isolated 4-PA using the global hybrid B3LYP functional, in combination with the def2-TZVP basis set. Thus, the experimental STM data provide further evidence that a surface reaction turns Bi4A into 4-PA. Temperature dependent STM studies suggest that at a temperature of 250 °C largest regions of highly ordered molecules were formed (Supporting Information, **Figure S9**).

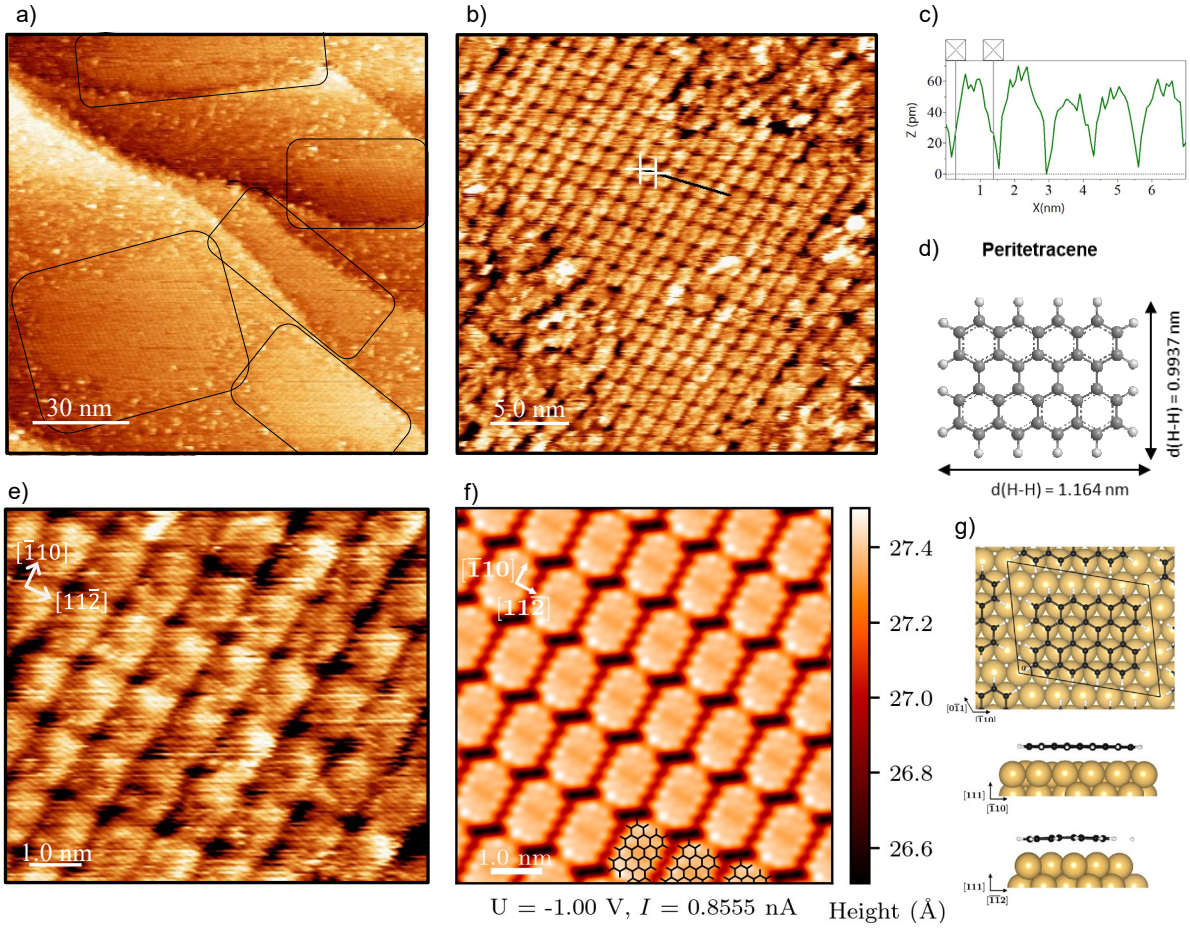

Figure 7: STM images of the annealed Bi4A monolayer/Cu (111): (a) annealed Bi4A islands of different domains (U = -0.2 V, I = 1 nA, measured at room temperature); (b) annealed monolayer coverage (U = -0.2 V, I = 1 nA, measured at room temperature); (c) topological profile; (d) calculated dimensions of 4-PA molecule; (e) zoom-in STM image of an annealed monolayer coverage Bi4A (U = -0.2 V, I = 1 nA, measured at room temperature); (f) simulated STM image; (g) structural model of the ideal adsorption place of 4-PA on Cu (111) from above (top) and aside (middle and bottom).

The adsorption geometry and proposed surface reaction is further supported by LEED, which probes larger, highly ordered surface areas. The experimental LEED pattern (**Figure 8a**) was recorded at a beam voltage of 18.5 eV at normal incidence of the electron beam. At this low beam energy, the spots represent the ordered molecular layer. A flower-like pattern of sharp LEED spots is clearly visible, indicating the formation of a highly ordered superstructure. The unit cell derived from the LEED pattern (**Figure 8b**) and calculations point to a 4-PA superstructure. The LEED pattern can be described in matrix notation by $\begin{pmatrix} 6 & -1 \\ -3 & 5 \end{pmatrix}$, as derived with the help of LEEDpat.[81]

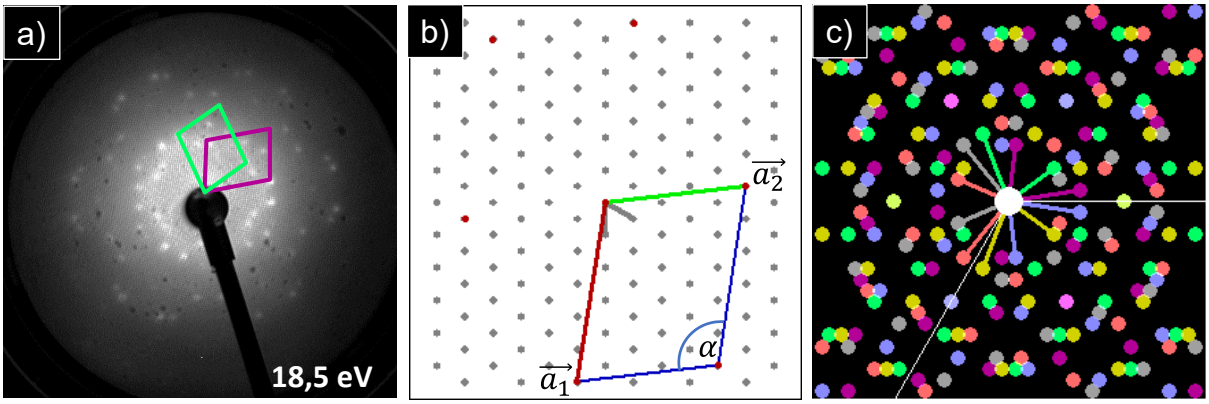

Figure 8: LEED image of an annealed Bi4A monolayer on Cu (111) at a beam energy of 18.5 eV (a), simulated lattice with unit cell defined by a_1 = 14.2 Å, a_2 = 11.1 Å, α = 105.54° (b) and corresponding simulated LEED pattern of a 4-PA molecule on a Cu (111) surface (c).

Due to the symmetry of the Cu (111) substrate there exist three rotational domains plus their inversion caused by the displacement of the molecule by one copper row at a time. These six rotational domains are indicated by different colors (**Figure 8c**). Due to the layer growth along the different domains, island formation on (111) surfaces is a well-known phenomenon. Complex LEED patterns on (111) surfaces with three rotational domains were also found for tetracene on Ag (111)[82-83] and Si (111).[84] While the LEED pattern of tetracene has a hexagonal shape, our pattern appears more like a six-petaled flower. The more square the unit cell becomes (and so the molecule), the more the LEED pattern changes from hexagonal to six-petaled.[85]

The experimental STM and LEED results are in excellent agreement with theoretical predictions. We calculated the adsorption geometry and electronic structure of Bi4A and 4-PA on Cu (111) at the level of density functional theory employing the repeated slab approach.[55]

For Bi4A / Cu (111) various starting geometries were tested. The optimal adsorption site is the hollow-hcp site with an $\begin{pmatrix} 7 & -1 \\ -3 & 6 \end{pmatrix}$ overlayer structure. It is important to note that the strong van-der-Waals interactions with the Cu (111) surface lead to a partial planarization of the molecule upon adsorption, however, the steric repulsion of the hydrogen atoms on neighboring arms of the molecule prevents the molecule from adsorbing in a completely flat configuration (see **Figure 1c** and **Figure S11**). The average adsorption distances of the carbon and hydrogen atoms are d_C = 2.95 ± 0.54 Å and d_H = 2.98 ± 0.67 Å, respectively, where we have defined the uncertainties in these numbers as standard deviations of individual atomic adsorption distances. Another measure for the non-planarity of the adsorption configuration of Bi4A / Cu (111) is given by the maximum out-of-plane displacement of the carbon atoms, $\Delta d = d_{C,max} - d_{C,min}$, for which we obtain a value of 1.81 Å.

The adsorption configuration of 4-PA / Cu (111), on the other hand, is computed to be almost entirely flat. Four adsorption sites on Cu (111) were tested as initial configuration, namely the top, bridge, hollow-fcc and hollow-hcp site. By calculating the adsorption energies of these four adsorption configurations, we determined the most favorable one, showing that 4-PA adsorbs in an almost flat configuration at the hollow-hcp site (see **Figure 7g**). The most-favorable adsorption geometry results in a $\begin{pmatrix} 6 & -1 \\ -3 & 5 \end{pmatrix}$ surface unit cell, in nice agreement with experimental LEED data. To ensure the system is not in a local minimum, additional calculations for 5° rotated molecules have

been performed, confirming the hollow-hcp site and the azimuthal orientation shown in **Figure 7g** as the most favorable adsorption configuration. Here, the average adsorption distances are d_C = 2.66 ± 0.06 Å for C atoms and d_H = 2.64 ± 0.05 Å for the H atoms, where the small standard deviations reflect the planar adsorption configuration. On close inspection, we identify a slight overall bending of the molecule along the armchair-edged axis which we quantify to be Δd = 0.22 Å defined in the same way as above. Based on the relaxed geometry, we simulated the STM using the Tersoff-Haman approximation[86-87] by assuming and a voltage of -1.0 eV. The resulting image (**Figure 7f**) is in excellent agreement with the experimental STM data (**Figure 7e**), confirming the formation of the planar 4-PA on Cu (111) upon annealing of Bi4A.

4. Conclusion

The molecule 1,1'-bitetracene (Bi4A) was synthesized for the first time and characterized by different spectroscopic techniques. The interface properties between Bi4A and Cu (111) was thoroughly studied by UPS, XPS, STM, LEED and DFT calculations. UPS and XPS measurements, together with DFT calculations, reveal a strong interaction with the copper surface of Bi4A and the annealed Bi4A (4-PA), which leads towards a planar geometry adsorption and a filled LUMO. The results reveal that Bi4A undergoes a cyclodehydrogenation to *peri*-tetracene (4-PA) on Cu (111) after annealing to 250 °C. 4-PA adsorbs along three rotational domains along the $[\bar{1}10]$-direction of the copper surface which results in an island formation. Thus, Bi4A can be regarded as a new precursor molecule for an on-surface reaction to 4-PA.

Author Contributions

The manuscript was written through contributions of all authors. All authors have given approval to the final version of the manuscript.

Conflicts of interest

There are no conflicts to declare.

Acknowledgments

The authors thank the Helmholtz-Zentrum Berlin (electron storage ring BESSY II) for provision of synchrotron radiation at the beamline PM4 and financial travel support. They acknowledge support by the state of Baden-Württemberg through bwHPC and the German Research Foundation (DFG) through Grant No. INST 40/575-1 FUGG (JUSTUS 2 cluster). The Center for Light-Matter Interaction, Sensors & Analytics (LISA+) at the University of Tübingen is acknowledged for technical support. N. K. and P. P. acknowledge the support from the European Research Council (ERC) Synergy Grant, Project ID 101071259. Part of the calculations have been performed on the Vienna Scientific Cluster (VSC).

ASSOCIATED CONTENT

Supporting Information: Synthesis route of 1,1'-bitetracene; additional ^{1}H and ^{13}C NMR spectra; additional STM and LEED data showing the gradual cyclodehydrogenation; DFT calculated adsorption site of Bi4A on Cu (111); additional peak fit data; corresponding energy-momentum ARPES intensity maps; additional energy level alignment; supplement experimental XAS spectra.

The Supporting Information is available free of charge at https://pubs.acs.org/

REFERENCES

1. Anthony, J. E., The Larger Acenes: Versatile Organic Semiconductors, *Angewandte Chemie-International Edition* **2008,** *47,* 452-483.
2. Bergenti, I.; Dediu, V.; Prezioso, M.; Riminucci, A., Organic Spintronics, *Philosophical Transactions of the Royal Society A: Mathematical, Physical and Engineering Sciences* **2011,** *369,* 3054-3068.
3. Lin, Y.-M.; Dimitrakopoulos, C.; Jenkins, K. A.; Farmer, D. B.; Chiu, H.-Y.; Grill, A.; Avouris, P., 100-Ghz Transistors from Wafer-Scale Epitaxial Graphene, *Science* **2010,** *327,* 662-662.
4. Jiang, D.-e.; Dai, S., Circumacenes Versus Periacenes: Homo–Lumo Gap and Transition from Nonmagnetic to Magnetic Ground State with Size, *Chemical Physics Letters* **2008,** *466,* 72-75.
5. Tönshoff, C.; Bettinger, H. F., Pushing the Limits of Acene Chemistry: The Recent Surge of Large Acenes, *Chemistry* **2021,** *27,* 3193-3212.
6. Anthony, J. E., Functionalized Acenes and Heteroacenes for Organic Electronics, *Chemical Reviews* **2006,** *106,* 5028-5048.
7. Liu, J.; Feng, X., Synthetic Tailoring of Graphene Nanostructures with Zigzag-Edged Topologies: Progress and Perspectives, *Angew Chem Int Ed Engl* **2020,** *59,* 23386-23401.
8. Ajayakumar, M. R.; Ma, J.; Feng, X., Π-Extended Peri-Acenes: Recent Progress in Synthesis and Characterization, *European Journal of Organic Chemistry* **2022,** *n/a,* e202101428.
9. Scholl, R.; Seer, C.; Weitzenbock, R., Perylene, a Highly Condensed Aromatic Hydrocarbon, C20h12, *Ber. Dtsch. Chem. Ges* **1910,** *43,* 2202-2209.
10. Clar, E., Das Kondensationsprinzip, Ein Einfaches Neues Prinzip Im Aufbau Der Aromatischen Kohlenwasserstoffe (Aromatische Kohlenwassertoffe Xlii. Mitteilung), *Chemische Berichte* **1948,** *81,* 52-63.
11. Roberson, L. B.; Kowalik, J.; Tolbert, L. M.; Kloc, C.; Zeis, R.; Chi, X.; Fleming, R.; Wilkins, C., Pentacene Disproportionation During Sublimation for Field-Effect Transistors, *Journal of the American Chemical Society* **2005,** *127,* 3069-3075.
12. Ajayakumar, M. R.; Fu, Y.; Ma, J.; Hennersdorf, F.; Komber, H.; Weigand, J. J.; Alfonsov, A.; Popov, A. A.; Berger, R.; Liu, J.; et al., Toward Full Zigzag-Edged Nanographenes: Peri-Tetracene and Its Corresponding Circumanthracene, *J Am Chem Soc* **2018,** *140,* 6240-6244.
13. Ni, Y.; Gopalakrishna, T. Y.; Phan, H.; Herng, T. S.; Wu, S.; Han, Y.; Ding, J.; Wu, J., A Peri-Tetracene Diradicaloid: Synthesis and Properties, *Angewandte Chemie International Edition* **2018,** *57,* 9697-9701.
14. Ajayakumar, M. R.; Ma, J.; Lucotti, A.; Schellhammer, K. S.; Serra, G.; Dmitrieva, E.; Rosenkranz, M.; Komber, H.; Liu, J.; Ortmann, F.; et al., Persistent Peri-Heptacene: Synthesis and in Situ Characterization, *Angewandte Chemie* **2021,** *133,* 13972-13977.
15. Zöphel, L.; Berger, R.; Gao, P.; Enkelmann, V.; Baumgarten, M.; Wagner, M.; Müllen, K., Toward the Peri-Pentacene Framework, *Chemistry – A European Journal* **2013,** *19,* 17821-17826.
16. Wang, X. Y.; Dienel, T.; Di Giovannantonio, M.; Barin, G. B.; Kharche, N.; Deniz, O.; Urgel, J. I.; Widmer, R.; Stolz, S.; De Lima, L. H.; et al., Heteroatom-Doped Perihexacene from a Double Helicene Precursor: On-Surface Synthesis and Properties, *J Am Chem Soc* **2017,** *139,* 4671-4674.
17. Fu, Y.; Chang, X.; Yang, H.; Dmitrieva, E.; Gao, Y.; Ma, J.; Huang, L.; Liu, J.; Lu, H.; Cheng, Z.; et al., Nbn-Doped Bis-Tetracene and Peri-Tetracene: Synthesis and Characterization, *Angewandte Chemie International Edition* **2021,** *60,* 26115-26121.
18. Wang, X.-Y.; Narita, A.; Zhang, W.; Feng, X.; Müllen, K., Synthesis of Stable Nanographenes with Obo-Doped Zigzag Edges Based on Tandem Demethylation-Electrophilic Borylation, *Journal of the American Chemical Society* **2016,** *138,* 9021-9024.
19. Siebrand, W., Radiationless Transitions in Polyatomic Molecules. Ii. Triplet-Ground-State Transitions in Aromatic Hydrocarbons, *The Journal of Chemical Physics* **2004,** *47,* 2411-2422.

20. Das, S.; Wu, J., Polycyclic Hydrocarbons with an Open-Shell Ground State, *Physical Sciences Reviews* **2017,** *2,* 20160109.
21. Shimizu, A.; Hirao, Y.; Kubo, T.; Nakano, M.; Botek, E.; Champagne, B. t., Theoretical Consideration of Singlet Open-Shell Character of Polyperiacenes Using Clar's Aromatic Sextet Valence Bond Model and Quantum Chemical Calculations, *AIP Conference Proceedings* **2012,** *1504,* 399-405.
22. Plasser, F.; Pašalić, H.; Gerzabek, M. H.; Libisch, F.; Reiter, R.; Burgdörfer, J.; Müller, T.; Shepard, R.; Lischka, H., The Multiradical Character of One- and Two-Dimensional Graphene Nanoribbons, *Angewandte Chemie International Edition* **2013,** *52,* 2581-2584.
23. Nakano, M., Open-Shell-Character-Based Molecular Design Principles: Applications to Nonlinear Optics and Singlet Fission, *Chem Rec* **2017,** *17,* 27-62.
24. Hachmann, J.; Dorando, J. J.; Avilés, M.; Chan, G. K.-L., The Radical Character of the Acenes: A Density Matrix Renormalization Group Study, *The Journal of Chemical Physics* **2007,** *127,* 134309.
25. Mishra, S.; Lohr, T. G.; Pignedoli, C. A.; Liu, J.; Berger, R.; Urgel, J. I.; Mullen, K.; Feng, X.; Ruffieux, P.; Fasel, R., Tailoring Bond Topologies in Open-Shell Graphene Nanostructures, *ACS Nano* **2018,** *12,* 11917-11927.
26. Rogers, C.; Chen, C.; Pedramrazi, Z.; Omrani, A. A.; Tsai, H. Z.; Jung, H. S.; Lin, S.; Crommie, M. F.; Fischer, F. R., Closing the Nanographene Gap: Surface-Assisted Synthesis of Peripentacene from 6,6'-Bipentacene Precursors, *Angew Chem Int Ed Engl* **2015,** *54,* 15143-15146.
27. Sanchez-Grande, A.; Urgel, J. I.; Veis, L.; Edalatmanesh, S.; Santos, J.; Lauwaet, K.; Mutombo, P.; Gallego, J. M.; Brabec, J.; Beran, P.; et al., Unravelling the Open-Shell Character of Peripentacene on Au(111), *J Phys Chem Lett* **2021,** *12,* 330-336.
28. Biswas, K.; Urgel, J. I.; Ajayakumar, M. R.; Ma, J.; Sánchez-Grande, A.; Edalatmanesh, S.; Lauwaet, K.; Mutombo, P.; Gallego, J. M.; Miranda, R.; et al., Synthesis and Characterization of Peri-Heptacene on a Metallic Surface, *Angewandte Chemie International Edition* **2022,** *61,* e202114983.
29. Urgel, J. I.; Mishra, S.; Hayashi, H.; Wilhelm, J.; Pignedoli, C. A.; Di Giovannantonio, M.; Widmer, R.; Yamashita, M.; Hieda, N.; Ruffieux, P.; et al., On-Surface Light-Induced Generation of Higher Acenes and Elucidation of Their Open-Shell Character, *Nature Communications* **2019,** *10,* 861.
30. Mishra, S.; Beyer, D.; Eimre, K.; Kezilebieke, S.; Berger, R.; Gröning, O.; Pignedoli, C. A.; Müllen, K.; Liljeroth, P.; Ruffieux, P.; et al., Topological Frustration Induces Unconventional Magnetism in a Nanographene, *Nature Nanotechnology* **2020,** *15,* 22-28.
31. Deniz, O.; Sánchez-Sánchez, C.; Dumslaff, T.; Feng, X.; Narita, A.; Müllen, K.; Kharche, N.; Meunier, V.; Fasel, R.; Ruffieux, P., Revealing the Electronic Structure of Silicon Intercalated Armchair Graphene Nanoribbons by Scanning Tunneling Spectroscopy, *Nano Letters* **2017,** *17,* 2197-2203.
32. Grimme, S.; Hansen, A.; Ehlert, S.; Mewes, J.-M., R2scan-3c: A “Swiss Army Knife” Composite Electronic-Structure Method, *The Journal of Chemical Physics* **2021,** *154,* 064103.
33. Björk, J.; Stafström, S.; Hanke, F., Zipping Up: Cooperativity Drives the Synthesis of Graphene Nanoribbons, *Journal of the American Chemical Society* **2011,** *133,* 14884-14887.
34. Yu, W.; Yoshii, T.; Aziz, A.; Tang, R.; Pan, Z.-Z.; Inoue, K.; Kotani, M.; Tanaka, H.; Scholtzová, E.; Tunega, D.; et al., Edge-Site-Free and Topological-Defect-Rich Carbon Cathode for High-Performance Lithium-Oxygen Batteries, *Advanced Science* **2023,** *10,* 2300268.
35. Xia, T.; Yoshii, T.; Nomura, K.; Wakabayashi, K.; Pan, Z.-Z.; Ishii, T.; Tanaka, H.; Mashio, T.; Miyawaki, J.; Otomo, T.; et al., Chemistry of Zipping Reactions in Mesoporous Carbon Consisting of Minimally Stacked Graphene Layers, *Chemical Science* **2023,** *14,* 8448-8457.
36. Niu, K. F.; Fan, Q. T.; Chi, L. F.; Rosen, J.; Gottfried, J. M.; Björk, J., Unveiling the Formation Mechanism of the Biphenylene Network, *Nanoscale Horizons* **2023,** *8,* 368-376.
37. Yeh, J. J.; Lindau, I., Atomic Subshell Photoionization Cross Sections and Asymmetry Parameters: $1 \leqslant Z \leqslant 103$, *Atomic Data and Nuclear Data Tables* **1985,** *32,* 1-155.
38. Seah, M. P.; Dench, W. A., Quantitative Electron Spectroscopy of Surfaces: A Standard Data Base for Electron Inelastic Mean Free Paths in Solids, *Surface and Interface Analysis* **1979,** *1,* 2-11.
39. Siegrist, T.; Kloc, C.; Schön, J. H.; Batlogg, B.; Haddon, R. C.; Berg, S.; Thomas, G. A., Enhanced Physical Properties in a Pentacene Polymorph, *Angewandte Chemie International Edition* **2001,** *40,* 1732-1736.

40. Hesse, R.; Chassé, T.; Streubel, P.; Szargan, R., Error Estimation in Peak-Shape Analysis of Xps Core-Level Spectra Using Unifit 2003: How Significant Are the Results of Peak Fits?, *Surface and Interface Analysis* **2004,** *36,* 1373-1383.
41. Schöll, A.; Zou, Y.; Jung, M.; Schmidt, T.; Fink, R.; Umbach, E., Line Shapes and Satellites in High-Resolution X-Ray Photoelectron Spectra of Large Pi-Conjugated Organic Molecules, *J Chem Phys* **2004,** *121,* 10260-10267.
42. Doniach, S.; Sunjic, M., Many-Electron Singularity in X-Ray Photoemission and X-Ray Line Spectra from Metals, *Journal of Physics C: Solid State Physics* **1970,** *3,* 285-291.
43. Giangrisostomi, E.; Ovsyannikov, R.; Sorgenfrei, F.; Zhang, T.; Lindblad, A.; Sassa, Y.; Cappel, U. B.; Leitner, T.; Mitzner, R.; Svensson, S.; et al., Low Dose Photoelectron Spectroscopy at Bessy Ii: Electronic Structure of Matter in Its Native State, *Journal of Electron Spectroscopy and Related Phenomena* **2018,** *224,* 68-78.
44. Horcas, I.; Fernández, R.; Gómez-Rodríguez, J. M.; Colchero, J.; Gómez-Herrero, J.; Baro, A. M., Wsxm: A Software for Scanning Probe Microscopy and a Tool for Nanotechnology, *Review of Scientific Instruments* **2007,** *78,* 013705.
45. Hermann, K. E.; Van Hove, M. A. Leedpat, Version 4.2. https://www.fhi.mpg.de/958975/LEEDpat4 (accessed Jan. 24, 2024).
46. Neese, F., The Orca Program System, *WIREs Computational Molecular Science* **2012,** *2,* 73-78.
47. Becke, A. D., Density-Functional Exchange-Energy Approximation with Correct Asymptotic Behavior, *Physical Review A* **1988,** *38,* 3098-3100.
48. Becke, A. D., Density-Functional Thermochemistry. Iii. The Role of Exact Exchange, *The Journal of Chemical Physics* **1993,** *98,* 5648-5652.
49. Weigend, F.; Ahlrichs, R., Balanced Basis Sets of Split Valence, Triple Zeta Valence and Quadruple Zeta Valence Quality for H to Rn: Design and Assessment of Accuracy, *Physical Chemistry Chemical Physics* **2005,** *7,* 3297-3305.
50. Kresse, G.; Furthmüller, J., Efficiency of Ab-Initio Total Energy Calculations for Metals and Semiconductors Using a Plane-Wave Basis Set, *Computational materials science* **1996,** *6,* 15-50.
51. Kresse, G.; Furthmüller, J., Efficient Iterative Schemes for Ab Initio Total-Energy Calculations Using a Plane-Wave Basis Set, *Physical review B* **1996,** *54,* 11169.
52. Kresse, G.; Joubert, D., From Ultrasoft Pseudopotentials to the Projector Augmented-Wave Method, *Physical review b* **1999,** *59,* 1758.
53. Perdew, J. P.; Burke, K.; Ernzerhof, M., Generalized Gradient Approximation Made Simple, *Physical review letters* **1996,** *77,* 3865.
54. Grimme, S., Semiempirical Gga-Type Density Functional Constructed with a Long-Range Dispersion Correction, *Journal of computational chemistry* **2006,** *27,* 1787-1799.
55. Neugebauer, J.; Scheffler, M., Adsorbate-Substrate and Adsorbate-Adsorbate Interactions of Na and K Adlayers on Al (111), *Physical Review B* **1992,** *46,* 16067.
56. Monkhorst, H. J.; Pack, J. D., Special Points for Brillouin-Zone Integrations, *Physical review B* **1976,** *13,* 5188.
57. Zhao, L.; Kaiser, R. I.; Lu, W. C.; Ahmed, M.; Evseev, M. M.; Bashkirov, E. K.; Azyazov, V. N.; Tonshoff, C.; Reicherter, F.; Bettinger, et al., A Free-Radical Prompted Barrierless Gas-Phase Synthesis of Pentacene, *Angewandte Chemie-International Edition* **2020,** *59,* 11334-11338.
58. Müller, U.; Roos, L.; Frank, M.; Deutsch, M.; Hammer, S.; Krumrein, M.; Friedrich, A.; Marder, T. B.; Engels, B.; Krueger, A.; et al., Role of Intermolecular Interactions in the Excited-State Photophysics of Tetracene and 2, 2'-Ditetracene, *The Journal of Physical Chemistry C* **2020,** *124,* 19435-19446.
59. Platt, J. R., Classification of Spectra of Cata-Condensed Hydrocarbons, *The Journal of chemical physics* **1949,** *17,* 484-495.
60. Jiro, T., The Electronic Spectra of Pyrene, Chrysene, Azulene, Coronene and Tetracene Crystals, *Bulletin of the Chemical Society of Japan* **1965,** *38,* 86-102.

61. Lukman, S.; Musser, A. J.; Chen, K.; Athanasopoulos, S.; Yong, C. K.; Zeng, Z.; Ye, Q.; Chi, C.; Hodgkiss, J. M.; Wu, J.; et al., Tuneable Singlet Exciton Fission and Triplet–Triplet Annihilation in an Orthogonal Pentacene Dimer, *Advanced Functional Materials* **2015,** *25,* 5452-5461.
62. Crispin, X.; Geskin, V.; Crispin, A.; Cornil, J.; Lazzaroni, R.; Salaneck, W. R.; Brédas, J.-L., Characterization of the Interface Dipole at Organic/ Metal Interfaces, *Journal of the American Chemical Society* **2002,** *124,* 8131-8141.
63. Franco-Cañellas, A.; Duhm, S.; Gerlach, A.; Schreiber, F., Binding and Electronic Level Alignment of Π-Conjugated Systems on Metals, *Reports on Progress in Physics* **2020,** *83,* 066501.
64. Braun, S.; Salaneck, W. R.; Fahlman, M., Energy-Level Alignment at Organic/Metal and Organic/Organic Interfaces, *Advanced Materials* **2009,** *21,* 1450-1472.
65. Wang, Q.; Yang, J.; Gerlach, A.; Schreiber, F.; Duhm, S., Advanced Characterization of Organic–Metal and Organic–Organic Interfaces: From Photoelectron Spectroscopy Data to Energy-Level Diagrams, *Journal of Physics: Materials* **2022,** *5,* 044010.
66. Derry, G. N.; Kern, M. E.; Worth, E. H., Recommended Values of Clean Metal Surface Work Functions, *J. Vac. Sci. Technol. A* **2015,** *33,* 060801.
67. Parashar, S.; Srivastava, P.; Pattanaik, M., Renormalization of Molecular Energy Levels in Single-Molecule Nanojunctions: An Ab-Initio Approach, *IOP Conference Series: Materials Science and Engineering* **2015,** *73*.
68. Bone, T. G.; Windischbacher, A.; Sattele, M. S.; Greulich, K.; Egger, L.; Jauk, T.; Lackner, F.; Bettinger, H. F.; Peisert, H.; Chasse, T.; et al., Demonstrating the Impact of the Adsorbate Orientation on the Charge Transfer at Organic-Metal Interfaces, *J Phys Chem C Nanomater Interfaces* **2021,** *125,* 9129-9137.
69. Ferretti, A.; Baldacchini, C.; Calzolari, A.; Di Felice, R.; Ruini, A.; Molinari, E.; Betti, M. G., Mixing of Electronic States in Pentacene Adsorption on Copper, *Phys. Rev. Lett.* **2007,** *99,* 4.
70. Baldacchini, C.; Allegretti, F.; Gunnella, R.; Betti, M. G., Molecule-Metal Interaction of Pentacene on Copper Vicinal Surfaces, *Surf. Sci.* **2007,** *601,* 2603-2606.
71. Koch, N.; Gerlach, A.; Duhm, S.; Glowatzki, H.; Heimel, G.; Vollmer, A.; Sakamoto, Y.; Suzuki, T.; Zegenhagen, J.; Rabe, J. P.; et al., Adsorption-Induced Intramolecular Dipole: Correlating Molecular Conformation and Interface Electronic Structure, *J. Am. Chem. Soc.* **2008,** *130,* 7300-7304.
72. Ules, T.; Luftner, D.; Reinisch, E. M.; Koller, G.; Puschnig, P.; Ramsey, M. G., Orbital Tomography of Hybridized and Dispersing Molecular Overlayers, *Phys Rev B* **2014,** *90,* 8.
73. Held, P. A.; Fuchs, H.; Studer, A., Covalent-Bond Formation Via on-Surface Chemistry, *Chemistry – A European Journal* **2017,** *23,* 5874-5892.
74. Otero, R.; Vázquez de Parga, A. L.; Gallego, J. M., Electronic, Structural and Chemical Effects of Charge-Transfer at Organic/Inorganic Interfaces, *Surface Science Reports* **2017,** *72,* 105-145.
75. Berkebile, S.; Puschnig, P.; Koller, G.; Oehzelt, M.; Netzer, F. P.; Ambrosch-Draxl, C.; Ramsey, M. G., Electronic Band Structure of Pentacene: An Experimental and Theoretical Study, *Phys Rev B* **2008,** *77,* 5.
76. Endo, O.; Matsui, F.; Kera, S.; Chun, W.-J.; Nakamura, M.; Amemiya, K.; Ozaki, H., Observation of Hole States at Perylene/Au(110) and Au(111) Interfaces, *J. Phys. Chem. C* **2022,** *126,* 15971-15979.
77. Sättele, M. S.; Windischbacher, A.; Greulich, K.; Egger, L.; Haags, A.; Kirschner, H.; Ovsyannikov, R.; Giangrisostomi, E.; Gottwald, A.; Richter, M.; et al., Hexacene on Cu(110) and Ag(110): Influence of the Substrate on Molecular Orientation and Interfacial Charge Transfer, *The Journal of Physical Chemistry C* **2022,** *126,* 5036-5045.
78. Alagia, M.; Baldacchini, C.; Betti, M. G.; Bussolotti, F.; Carravetta, V.; Ekström, U.; Mariani, C.; Stranges, S., Core-Shell Photoabsorption and Photoelectron Spectra of Gas-Phase Pentacene: Experiment and Theory, *The Journal of Chemical Physics* **2005,** *122,* 124305.
79. Grüninger, P.; Polek, M.; Ivanović, M.; Balle, D.; Karstens, R.; Nagel, P.; Merz, M.; Schuppler, S.; Ovsyannikov, R.; Bettinger, H. F.; et al., Electronic Structure of Hexacene and Interface Properties on Au(110), *The Journal of Physical Chemistry C* **2018,** *122,* 19491-19498.
80. Simonov, K. A.; Vinogradov, N. A.; Vinogradov, A. S.; Generalov, A. V.; Zagrebina, E. M.; Svirskiy, G. I.; Cafolla, A. A.; Carpy, T.; Cunniffe, J. P.; Taketsugu, T.; et al., From Graphene

Nanoribbons on Cu(111) to Nanographene on Cu(110): Critical Role of Substrate Structure in the Bottom-up Fabrication Strategy, *ACS Nano* **2015,** *9,* 8997-9011.
81. *Leedpat*, 4.2; 2014.
82. Langner, A.; Hauschild, A.; Fahrenhoz, S.; Sokolowski, M., Structural Properties of Tetracene Films on Ag(111) Investigated by Spa-Leed and Tpd, *Surface Science* **2005,** *574,* 153-165.
83. Soubatch, S.; Kröger, I.; Kumpf, C.; Tautz, F. S., Structure and Growth of Tetracene on Ag(111), *Physical Review B* **2011,** *84,* 195440.
84. Jaeckel, B.; Lim, T.; Klein, A.; Jaegermann, W.; Parkinson, B. A., Deposition of Tetracene on Gase Passivated Si(111), *Langmuir* **2007,** *23,* 4856-4861.
85. Wang, Q.; Yang, J. C.; Franco-Canellas, A.; Burker, C.; Niederhausen, J.; Dombrowski, P.; Widdascheck, F.; Breuer, T.; Witte, G.; Gerlach, A.; et al., Pentacene/Perfluoropentacene Bilayers on Au(111) and Cu(111): Impact of Organic-Metal Coupling Strength on Molecular Structure Formation, *Nanoscale Advances* **2021,** *3,* 2598-2606.
86. Tersoff, J.; Hamann, D. R., Theory of the Scanning Tunneling Microscope, *Physical Review B* **1985,** *31,* 805.
87. Heimel, G.; Romaner, L.; Zojer, E.; Brédas, J.-L. In *A Theoretical View on Self-Assembled Monolayers in Organic Electronic Devices*, Organic Optoelectronics and Photonics III, SPIE: 2008; pp 197-208.

TOC Graphic